



# NIH Public Access

## Author Manuscript

Biochemistry. Author manuscript; available in PMC 2014 May 21.

Published in final edited form as:

*Biochemistry*. 2013 May 21; 52(20): . doi:10.1021/bi400322e.

## Side-Chain Conformational Heterogeneity of Intermediates in the *Escherichia coli* Dihydrofolate Reductase Catalytic Cycle

Lisa M. Tuttle, H. Jane Dyson, and Peter E. Wright\*

Department of Integrative Structural and Computational Biology and Skaggs Institute for Chemical Biology, The Scripps Research Institute, 10550 North Torrey Pines Road, La Jolla, California 92037

### Abstract

*Escherichia coli* dihydrofolate reductase (DHFR) provides a paradigm for the integrated study of the role of protein dynamics in enzyme function. Previous studies of backbone and side chain dynamics have yielded unprecedented insights into the mechanism by which DHFR progresses through the structural changes that occur during its catalytic cycle. Here we report a comprehensive study of the  $\chi_1$  rotamer populations of the aromatic and  $\gamma$ -methyl containing residues for complexes of the catalytic cycle, based on NMR measurement of  $^3J_{C\gamma CO}$  and  $^3J_{C\gamma N}$  coupling constants. We report conformational and dynamic information for eight distinct complexes, where transitions between rotamer wells may occur on a broad picosecond to millisecond timescale. This large volume of  $^3J$  data has allowed us to fit new Karplus parameterizations for aromatic side chains, and to select the best available of previously determined parameters for Ile, Thr, and Val. The  $^3J_{C\gamma CO}$  and  $^3J_{C\gamma N}$  coupling constants are found to be extremely sensitive measures of side chain  $\chi_1$  rotamers, and to give important insights into the extent of conformational averaging. For a subset of residues in DHFR, the extent of rotamer averaging is invariant to the nature of the bound ligand, while for other residues the rotamer averaging differs in one or more complexes of the enzymatic cycle. These variable-averaging residues are generally located near the active site, but the phenomenon extends into the adenosine binding domain. For several residues, the rotamer populations in different DHFR complexes appear to depend on whether the complex is in the closed or occluded state, and some residues are exquisitely sensitive to small changes in the nature of the bound ligand.

### Keywords

NMR; coupling constant; rotamer; Karplus parameters

Dihydrofolate reductase (DHFR) is an essential enzyme found in all organisms and many viruses. It catalyzes the reduction of 7,8-dihydrofolate (DHF) to (6S)-5,6,7,8-tetrahydrofolate (THF) using reduced nicotinamide adenine dinucleotide phosphate (NADPH) as a cofactor. *E. coli* DHFR is a 159-residue protein composed of an 8-stranded  $\beta$ -sheet (designated  $\beta$ A- $\beta$ H), four  $\alpha$ -helical regions ( $\alpha$ B,  $\alpha$ C,  $\alpha$ E,  $\alpha$ F), and connecting

\*Corresponding Author: Department of Integrative Structural and Computational Biology and Skaggs Institute for Chemical Biology, The Scripps Research Institute, 10550 North Torrey Pines Road, La Jolla, California 92037. Telephone: (858) 784-9721. Fax: (858) 784-9822. wright@scripps.edu.

The authors declare no competing financial interest.

#### SUPPORTING INFORMATION AVAILABLE

Tables showing complete rotamer populations and  $^3J_{C\gamma CO}$  and  $^3J_{C\gamma N}$  coupling constants for each of the complexes, supplementary figures and detailed descriptions of the behavior of a number of residues. Supporting materials may be accessed free of charge online at <http://pubs.acs.org>.

loops.<sup>1–3</sup> The active site lies in a deep hydrophobic cleft that divides the protein into two subdomains: the adenosine binding subdomain (residues 38–106) and the loop subdomain (Figure 1A). The loop subdomain contains residues from the C- and N-termini and includes three functionally important loop regions: the Met20 loop (residues 9–24), the F-G loop (residues 116–132), and the G-H loop (residues 142–150).<sup>4</sup> The Met20 loop has been observed in three distinct configurations: closed, occluded, and open. Figure 1A shows a structural superposition with the position of the Met20 loop in the closed configuration shown in blue (corresponding to the fully-bound NADP<sup>+</sup> in light blue), while the occluded configuration is shown in red (corresponding to the red NADP<sup>+</sup> with the nicotinamide ring flipped out of the pocket). The catalytic cycle of the enzyme (E), illustrated in Figure 1B, proceeds through five kinetically observable intermediates: the Michaelis complex E:DHF:NADPH (modeled by E:FOL:NADP<sup>+</sup>, containing the pseudosubstrate folate), the product ternary complex E:THF:NADP<sup>+</sup>, the product binary complex E:THF, the product release complex E:THF:NADPH, and the holoenzyme E:NADPH. Additionally, the complex with the drug methotrexate (E:MTX:NADPH) has been proposed to represent a model for the transition state between the Michaelis complex and the product ternary complex.<sup>3</sup> The Met20 loop is in a closed configuration in the holoenzyme, the Michaelis complex, and the transition state model, and is in an occluded conformation in the product complexes. E:FOL has frequently been used as a model for E:THF, but results described here and elsewhere,<sup>5</sup> increasingly demonstrate the exquisite sensitivity of *E. coli* DHFR to the bound substrate, and we therefore use the product (THF) binary complex itself, despite the experimental difficulties caused by the instability of THF towards air and light.

In traversing the catalytic cycle, *E. coli* DHFR undergoes significant loop and backbone motions.<sup>6</sup> Side chain motions also contribute substantially to the configurational entropy of the system.<sup>7–9</sup> Primary methods for probing backbone and side chain dynamics include NMR relaxation studies, x-ray crystallography (through temperature factors and room temperature structure determination<sup>10</sup>), and computer simulations.<sup>3,6,11–13</sup> Although side chain rotamer populations do not provide direct information on the timescale at which the rotamer averaging takes place, the observation of differences in rotamer populations between complexes in the DHFR catalytic cycle gives important information on a possible cross section of motions that occur with timescales spanning from picosecond to millisecond.<sup>14</sup>

For amino acids with side chains that extend beyond C $\beta$ , different orientations of the side chain, associated with variations in the  $\chi_1$  dihedral angle, can result in substantial changes in local structure. The 3-bond coupling constants between the C $\gamma$  of an amino acid side chain and the backbone carbonyl carbon or amide nitrogen of the same residue ( $^3J_{C\gamma CO}$  and  $^3J_{C\gamma N}$  respectively) describe the orientation of the side chain with respect to the backbone, determined by the  $\chi_1$  dihedral angle (Figure 1C). NMR measurements of the  $^3J_{C\gamma CO}$  and  $^3J_{C\gamma N}$  coupling constants therefore provide information on the  $\chi_1$  dihedral angle sampled in solution. Extensive rotamer libraries based on x-ray structures show that side chain  $\chi_1$  dihedral angles have non-overlapping distributions about the staggered rotamer conformations centered at *trans* (180°), *gauche*<sup>+</sup> (+60°), and *gauche*<sup>-</sup> (−60°).<sup>15</sup> The assumption of a 3-site jump model is further supported by x-ray crystallographic studies which show that with increasing resolution, there is a systematic tendency for  $\chi_1$  angles to approach the three canonical rotamer angles.<sup>16,17</sup> Non-canonical rotamers are only rarely observed in high resolution x-ray structures (<1%) and those that are observed are due to a highly restricted conformational state where clashes would occur in each of the *trans*, *gauche*<sup>+</sup>, and *gauche*<sup>-</sup> conformations, with such situations most likely to occur for bulky aromatic side chains.<sup>17</sup> Comparison of the experimental  $^3J$  couplings to expected values described by Karplus curves gives information on the dominant  $\chi_1$  rotamers.<sup>18,19</sup> Deviations from the expected values arise from sampling of multiple rotamers, which can be described

using a 3-site jump model<sup>20,21</sup> or from restricted conformational sampling within a single rotamer energy well. The propensity of a side chain to undergo either rotamer hopping or motions within a rotamer well is dependent on the packing density around the side chain and the conformational dynamics of neighboring residues or ligands. When rotamer hopping is the dominant contribution to conformational averaging, Karplus parameters allow the  $^3J_{C\gamma CO}$  and  $^3J_{C\gamma N}$  couplings to be converted into rotamer populations for each of the staggered rotamers. Minor rotamer populations can have functional significance. For proline isomerase, for example, room temperature crystallography has shown that minor rotamers of active site residues are important for promotion of catalysis.<sup>22</sup>

In the work presented here, the solution state  $\chi_1$  rotamer populations for 20 aromatic residues (Phe, Tyr, Trp, His) and 29  $\gamma$ -methyl containing residues (Ile, Thr, Val) were determined for the five intermediates formed in the steady state *E. coli* DHFR enzymatic cycle, together with a putative transition state model (E:MTX:NADPH) and the pseudo-substrate binary complex E:FOL, which is included for comparison with the true product binary complex E:THF. Finally, to determine the possible effect of  $\mu$ s-ms timescale backbone motions on the measured  $^3J$  values, and therefore on the calculated rotamer populations, the coupling constants for the wild type E:FOL:NADP<sup>+</sup> complex, which undergoes ms timescale fluctuations in the active site loops, are compared to those for the mutant N23PP/S148A in which these fluctuations are abrogated.<sup>23</sup> Additional information is obtained from estimates of Leu  $\chi_2$  side chain rotamer averaging, predicted from the  $^{13}C$  methyl chemical shifts for each complex.<sup>24</sup>

Although the degree of rotamer averaging for most residues is unchanged throughout the enzymatic cycle, a number of side chains display different rotamer averaging behavior in the various complexes of DHFR. Differences in the extent of rotamer averaging are observed primarily near the active site, but also at sites in the adenosine binding domain. For several residues, variation of the rotamer populations between complexes depends on whether the complex is in the closed or occluded state, whereas for other side chains the variation of rotamer populations between complexes is more dependent on the presence or absence of ligands. Overall, methyl side chains tend to have a basal level of conformational averaging at room temperature, whereas buried aromatic side chains are much more likely to populate a single predominant rotamer conformation. These differences reflect the greater volume of the aromatic side chains compared to the methyl-containing side chains, and reveal important insights into the role of side chain heterogeneity in the mechanism of enzyme action.

## MATERIALS AND METHODS

### Protein Purification and Sample Preparation

Wild type and mutant N23PP/S148A *E. coli* DHFR were overexpressed in BL21 (DE3) (DNAY) cells in M9 minimal medium. Samples for assignments and  $^3J$  coupling experiments were uniformly  $^{13}C$ ,  $^{15}N$ -labeled and were purified as described previously.<sup>25</sup> NADPH and THF are light and air sensitive, and all samples containing these ligands were prepared in an argon-equilibrated glove box. The NMR buffer was thoroughly degassed under vacuum through a freeze-pump-thaw cycle and the protein was exchanged into NMR buffer [pH 7.6, 70 mM KPi, 25 mM KCl, 1 mM EDTA, 1 mM DTT, 10% D<sub>2</sub>O]. Final sample concentrations ranged from 1–3 mM. Complexes were formed by addition of 6-fold excess of substrate [FOL, THF, or MTX] and 10-fold excess of cofactor [NADP<sup>+</sup> or NADPH]. The sample was further degassed on a vacuum line, overlaid with argon, and flame sealed in an amberized tube. E:THF:NADP<sup>+</sup>, E:THF:NADPH, and E:NADPH samples are only stable for 1–2 weeks under experimental conditions; several fresh samples were required to complete the three or more trials for measuring  $^3J$  coupling constants. Since

DHFR is extremely sensitive to the bound ligands, it is essential to use highly pure ligand of the appropriate stereochemistry. (6*S*)-THF was purchased from Schircks Laboratories, and high purity NADPH and NADP<sup>+</sup> were purchased from Sigma.

### Side Chain and Backbone Resonance Assignments

Methyl resonance assignments for wild type E:FOL:NADP<sup>+</sup> and E:FOL were reported previously.<sup>9</sup> Assignments for other complexes were made using <sup>13</sup>C-HSQC<sup>26</sup> and (H)C(CO)NH/H(CCO)NH<sup>27</sup> experiments. Backbone amide assignments were completed using standard HNCA and HN(CO)CA experiments.<sup>28</sup> All spectra for assignments and coupling constant measurements were recorded at 301 K at a <sup>1</sup>H spectrometer frequency of 600 MHz.

### Measurement of Methyl <sup>3</sup>J<sub>C<sub>γ</sub>CO</sub> and <sup>3</sup>J<sub>C<sub>γ</sub>N</sub>

Experiments to measure <sup>3</sup>J<sub>C<sub>γ</sub>CO</sub> and <sup>3</sup>J<sub>C<sub>γ</sub>N</sub> coupling constants for Ile, Thr, and Val  $\gamma$ -methyl groups were adapted from previously developed spin-echo difference <sup>13</sup>C-HSQC experiments<sup>29,30</sup> by addition of a shaped 180° <sup>13</sup>CO pulse so that the same reference experiment could be used for both <sup>3</sup>J<sub>C<sub>γ</sub>CO</sub> and <sup>3</sup>J<sub>C<sub>γ</sub>N</sub> measurements. The modified pulse sequence is shown in Supplementary Figure S1. Data were acquired in an interleaved manner, in triplicate or greater for each complex. The values for the <sup>3</sup>J<sub>C<sub>γ</sub>CO</sub> or <sup>3</sup>J<sub>C<sub>γ</sub>N</sub> couplings were calculated for each residue by comparing the intensity of cross peaks in the spin-echo difference spectrum with the intensity of the corresponding cross peak in a reference spectrum. Coupling constants for methyl-containing residues were calculated using the relationship  $(I_a - I_b)/I_a = 2 \sin^2(\pi J_{C\gamma X} T)$ , where  $I_a$  is the reference spectrum intensity,  $I_b$  is the intensity in the spin-echo difference spectrum and the constant time evolution  $T$  was 28.6 ms. In a previous application of these coupling constant measurements to the E:FOL:NADP<sup>+</sup> and E:FOL complexes,<sup>9</sup> there was a systematic reduction in the magnitude of <sup>3</sup>J<sub>C<sub>γ</sub>CO</sub>, apparently due to an improperly calibrated <sup>13</sup>C carbonyl inversion pulse, leading to errors in rotamer populations for some residues. In the current experiments, this pulse has been replaced by a Q3 shaped pulse, which is far less sensitive to small errors in calibration. The accuracy of the modified pulse scheme has been verified using human ubiquitin, where it faithfully reproduced published coupling constants.<sup>31</sup>

### Measurement of Aromatic <sup>3</sup>J<sub>C<sub>γ</sub>CO</sub> and <sup>3</sup>J<sub>C<sub>γ</sub>N</sub>

Experiments to measure <sup>3</sup>J<sub>C<sub>γ</sub>CO</sub> and <sup>3</sup>J<sub>C<sub>γ</sub>N</sub> coupling constants for His, Phe, Trp, and Tyr residues were adapted from previously developed spin-echo difference <sup>15</sup>N-HSQC experiments,<sup>32</sup> with coupling and reference experiments collected in an interleaved manner. All <sup>3</sup>J measurements were made in triplicate or more. The coupling constants were calculated from the relationship  $I_b/I_a = \cos(2\pi J_{C\gamma X} T)$ , where  $I_a$  is the reference spectrum intensity and  $I_b$  is the intensity for the amide of the  $i+1$  residue in the <sup>3</sup>J<sub>C<sub>γ</sub>CO</sub> experiment or for the  $i$  residue in the <sup>3</sup>J<sub>C<sub>γ</sub>N</sub> experiment. The constant time evolution  $T$  was 25 ms for <sup>3</sup>J<sub>C<sub>γ</sub>CO</sub> experiments and 50 ms for <sup>3</sup>J<sub>C<sub>γ</sub>N</sub> experiments. Since the <sup>3</sup>J<sub>C<sub>γ</sub>CO</sub> measurement for aromatic side chains depends on the amide resonance of the next residue, <sup>3</sup>J<sub>C<sub>γ</sub>CO</sub> values are not available when the  $i+1$  residue is a proline.

### Derivation of Karplus Parameters from DHFR Aromatic Couplings

The only available published Karplus parameters for aromatic residues<sup>19,33</sup> gave poor fits to the <sup>3</sup>J<sub>C<sub>γ</sub>CO</sub> and <sup>3</sup>J<sub>C<sub>γ</sub>N</sub> measured for the complexes of DHFR. Specifically, the maximum and minimum values, which in many cases should represent the coupling constant expected for a rotamer populated at ~100%, were poorly estimated. The availability of a series of excellent x-ray crystal structures, representing all of the complexes studied in this report, together with nearly complete coupling constant data for the aromatic residues in each complex,

suggested the calculation of a new set of Karplus parameters more suited to the tightly-packed aromatic side chains encountered in the DHFR complexes (see Results).

The aromatic  $^3J_{C\gamma CO}$  and  $^3J_{C\gamma N}$  coupling constants used for the calculation were selected on the basis of an inspection of the structures. Only side chains tightly packed in the interior of the complexes were used, and these were further selected to contain only those residues where the two coupling constants were both consistent with the presence of a single rotamer. The Karplus parameters  $A$ ,  $B$  and  $C$  and the phase offset  $\delta$  calculated by least-squares fit to the Karplus equation (see Eq. 5) are shown in Table 1A.

### Calculation of $\chi_1$ Rotamer Populations from Coupling Constants

For each residue, the  $\chi_1$  rotamer populations were calculated from the values of the  $^3J_{C\gamma CO}$  and  $^3J_{C\gamma N}$  coupling constants, assuming a 3-site jump model, using the following equations:<sup>34</sup>

$$^3J_{exp,C\gamma N} = p_{180} ^3J_{t,C\gamma N} + p_{+60} ^3J_{g,C\gamma N} + p_{-60} ^3J_{h,C\gamma N} \quad (1)$$

$$^3J_{exp,C\gamma CO} = p_{180} ^3J_{t,C\gamma CO} + p_{+60} ^3J_{g,C\gamma CO} + p_{-60} ^3J_{h,C\gamma CO} \quad (2)$$

$$p_{180} + p_{+60} + p_{-60} = 1 \quad (3)$$

where  $^3J_{exp,C\gamma N}$  and  $^3J_{exp,C\gamma CO}$  are the experimentally measured coupling constants;  $p_{-60}$ ,  $p_{60}$ , and  $p_{180}$  are the populations of the respective  $\chi_1$  rotamer states; and  $J_t$ ,  $J_g$ , and  $J_h$  for  $C\gamma CO$  and  $C\gamma N$  are the expected coupling values for the fully populated  $180^\circ$ ,  $+60^\circ$ , and  $-60^\circ$   $\chi_1$  rotamers, respectively. Choice of Karplus parameters has a large impact on the calculated rotamer populations, and the new Karplus parameters derived from the aromatic couplings measured in this study were used throughout the calculation. The residue dependent  $J_t$ ,  $J_g$ , and  $J_h$  values chosen are given in Table 1B, with the appropriate phase shifts made so that all values are with respect to the  $\chi_1$  angle (e.g.,  $^3J_{C\gamma N}$  for Ile has a maximum when  $\theta(N\text{-CA}\text{-CB}\text{-C}\gamma 2)$  is  $180^\circ$ ; this corresponds to the  $-60^\circ$   $\chi_1$  angle).

Rotamer populations were calculated using Eqs. 1–3 and the  $J_t$ ,  $J_g$ , and  $J_h$  values of Table 1B. The final rotamer populations were normalized to fall between 0 and 1. For valine, when coupling measurements for both  $C\gamma 1$  and  $C\gamma 2$  methyl groups are available, the rotamer populations represent an average of the populations obtained. Population ranges were determined using  $^3J \pm \sigma$ , where  $\sigma$  is the standard deviation based on the three or more measurements of  $^3J$ ; this range is, in general, not symmetric about the average population. Note that small values of  $^3J$  are prone to larger percent errors when the primary contribution to error is from noise in the NMR spectra. For some residues, particularly the aromatic side chains, the  $^3J$  values clearly do not report on rotamer jumps, but instead reflect either a non-classical rotamer, or more likely are indicative of conformational sampling within a single rotamer well. Since the coupling constants alone do not allow us to distinguish local fluctuations within a single rotamer well from a process that involves jumps between two or more rotamer wells, it is necessary to interpret the  $^3J$  coupling values within the context of the three-dimensional structure of each complex [E:NADPH (1RX1), E:FOL:NADP<sup>+</sup> (3QL3 and 1RX2), E:MTX:NADPH (1RX3), E:THF:NADP/H (1RX4), E:THF (1RX5), E:FOL (1RX7), and N23PP/S148A E:FOL:NADP<sup>+</sup> (3QL0)].<sup>3,23</sup> The propensity of a side chain to sample a certain  $\chi_1$  rotamer is dependent on the residue type and the backbone conformation. For reference, Figure S2 shows plots of the DHFR  $\phi$ ,  $\psi$  values for the E:FOL:NADP<sup>+</sup> complex (3QL3) overlaid on plots of the backbone dependent rotamer

populations according to Shapovalov and Dunbrack<sup>15</sup> for the aromatic, Val, Thr, and Ile residues.

### Calculation of Leucine $\chi_2$ Rotamer Populations from Chemical Shifts

For leucines, a simple relationship between the chemical shifts of the methyl carbons has been reported as

$$\Delta\delta(^{13}C) = ^{13}C_{\delta 1} - ^{13}C_{\delta 2} = -5 + 10 \bullet p_{180} \quad (4)$$

where  $p_{180}$  is the population of the  $\chi_2 = 180^\circ$  rotamer.<sup>24</sup> Despite the nine possible  $\chi_1, \chi_2$  pairs for leucine, only two of these are significantly sampled in the PDB: (180, +60) and (-60, 180).<sup>15</sup> Therefore, knowledge of the  $\chi_2$  rotamer is largely predictive of the  $\chi_1$  rotamer conformation. To minimize the influence of neighboring aromatic side chains or ligand, we subtract the aromatic contribution to each methyl shift as determined from Shifts-4.3<sup>35</sup> using each of the applicable x-ray structures.

## RESULTS

### Measurement of $^3J_{C\gamma CO}$ and $^3J_{C\gamma N}$ Coupling Constants

The coupling constants used to estimate  $\chi_1$  rotamer populations are derived from the intensities of cross peaks in spin-echo difference NMR spectra. A representative data set is shown in Figure 2. Comparison of the intensities of cross peaks in the  $C\gamma CO$  or the  $C\gamma N$  spectra with the corresponding cross peaks in a reference HSQC spectrum yields values of the  $^3J_{C\gamma CO}$  or  $^3J_{C\gamma N}$  coupling constants that are used to calculate populations of the three canonical  $\chi_1$  rotamers according to Equations 1–3, or in some cases, are correlated to side chain motions within a single rotamer well. A total of 8 different complexes of *E. coli* DHFR were studied, each yielding data for 11 valines, 12 isoleucines, 6 threonines, 6 phenylalanines, 4 tyrosines, 5 tryptophans, and 5 histidines. The  $^3J_{C\gamma CO}$  and  $^3J_{C\gamma N}$  coupling constants measured for each complex are given in Supplementary Tables S2–S9 for Val, Ile, and Thr, and Supplementary Tables S11–S18 for Phe, Tyr, Trp, and His. Average values over all complexes, which are useful in gauging the extent of rotamer differences between complexes for each residue, are given in Supplementary Tables S1 and S10.

### Re-Parameterization of Karplus Curves Using Experimental Data

The general form of the Karplus relationship is

$$J = A \cos^2(\theta + \delta) + B \cos(\theta + \delta) + C \quad (5)$$

where  $A$ ,  $B$ , and  $C$  are the Karplus parameters;  $\theta$  is the dihedral angle; and  $\delta$  is a phase offset. When  $\delta$  is zero, the curves are symmetric about the maximum value. However, since many amino acid side chains are chiral (or in the case of residues such as valine, prochiral, with two methyl groups that are chemically equivalent but not sterically equivalent), the configuration of atoms for the dihedral angles giving minima in the Karplus relationship are not mirror images of each other, and so different minimum coupling values are to be expected, resulting in asymmetric Karplus curves with a non-zero phase shift  $\delta$ .<sup>19</sup> In the absence of motional averaging, the Karplus curve would describe the  $^3J$  coupling value for any given dihedral angle. However, Karplus relationships are empirically derived from experimental  $^3J$  values that necessarily reflect dynamic effects arising from the thermal energy in a system, as demonstrated by Case and coworkers.<sup>36</sup>

Two sets of Karplus parameters for  $\chi_1$  are available in the literature. One set uses  $^3J$  measurements of *D. vulgaris* flavodoxin to determine Karplus parameters for each of the  $^3J$  couplings defining the  $\chi_1$  angle for all residue types.<sup>19,33</sup> However, based on our numerous  $^3J$  measurements for *E. coli* DHFR complexes, we find that the flavodoxin-based parameters significantly underestimate the maxima in the Karplus curves, particularly for aromatic residues. This is likely due to the location of many of the flavodoxin aromatic residues in loosely packed regions of the protein, where more motional averaging can be expected.

Since the agreement between our data and the published Karplus parameters for aromatic side chains is so poor, we decided to utilize a limited set of our own coupling constant data, excluding residues that could potentially be subject to rotamer averaging, to determine new Karplus parameters for which the maximum  $^3J$  values better estimate those observed in our experiments. Many of the aromatic side chains in DHFR are in tightly packed locations where sampling of multiple rotamers is not expected to occur. Based on the  $^3J$  couplings of these motionally restricted aromatic side chains, we have determined new Karplus parameters according to Eq. 5, by performing a least squares fit using the measured couplings and the corresponding x-ray  $\chi_1$  angle (Figure 3). Residues were excluded from the fit if the error in either coupling constant measurement was > 1.0 Hz or if both  $^3J_{C\gamma CO}$  and  $^3J_{C\gamma N}$  couplings constants were less than  $0.9 * \text{max}[J(180), J(-60)]$ . Data for residues with  $+60^\circ$  rotamers were included except for Trp22, which appears to undergo fluctuations within its major  $\chi_1$  rotamer well (see Supplemental Information). Additionally, His45, which has exceptionally large  $^3J_{C\gamma CO}$  values, was excluded from the fits for histidine Karplus parameters. Excluded pairs of couplings are shown as open circles in Figure 3; filled circles indicate data used in the re-parameterization. The large number of data points at each of the staggered rotamers for Phe, Trp, and Tyr residues (FWY) in DHFR were fit together. While the Karplus curves for aromatic residues are expected to be at least somewhat asymmetric, we could not justify fitting a non-zero  $\delta$  in the absence of additional data. Fewer reliable  $^3J$  couplings were available for histidine residues in *E. coli* DHFR complexes, and since these all have an expected  $-60^\circ$   $\chi_1$  rotamer, we used additional His  $^3J$  data from human DHFR, which included  $180^\circ$   $\chi_1$  rotamers. Due to the limited His data, we restrained the *A* and *B* Karplus parameters to those determined from the FWY fit, varying only *C*, as was done by Schmidt and coworkers.<sup>19,33</sup> The resultant Karplus parameters are given in Table 1A. An illustration of the agreement of our newly derived parameters with available published  $\chi_1$  data is shown in Figure S3.

A second set of published Karplus parameters for  $\chi_1$  of the  $\gamma$ -methyl containing residues Ile, Thr, and Val used DFT simulations and comparison to experimental dipolar coupling data on human ubiquitin and protein GB3 to determine the  $^3J_{C\gamma CO}$  and  $^3J_{C\gamma N}$  Karplus parameters.<sup>14</sup> Reasonable agreement is seen between these Karplus curves and the DHFR coupling data for  $^3J_{C\gamma CO}$  and  $^3J_{C\gamma N}$  of Thr,  $^3J_{C\gamma N}$  of Val, and  $^3J_{C\gamma CO}$  of Val-C $\gamma$ 2 (Figures S3 and S4). However, our  $^3J_{C\gamma CO}$  data for Val-C $\gamma$ 1 (Figure S4) do not reflect as large a phase shift as determined by the DFT parameters<sup>14</sup> but fit better to the  $^3J_{C\gamma CO}$  Val-C $\gamma$ 2 DFT curve. Given the slight, but systematic differences in the  $\chi_1$  rotamer populations determined for Val-C $\gamma$ 1 and Val-C $\gamma$ 2, it is probable that these probes should have unique  $^3J_{C\gamma CO}$  Karplus parameters. The same parameters as were used for Val-C $\gamma$ 2 also provide a better fit for the Ile  $^3J$  data than did the ‘Ile/Val Best Fit’ curves.<sup>14</sup> However, our DHFR data suggest that the expectation value for Ile  $^3J_{C\gamma N}$  at  $\chi_1 = +60^\circ$  should be somewhat larger than the 0.31 Hz associated with the Val-C $\gamma$ 2 Karplus parameters. The resulting expected  $^3J$  values for the fully populated staggered rotamers ( $J_t$ ,  $J_g$ , and  $J_h$  of Eqs. 1–3) for each residue type are given in Table 1B.

The values of the  ${}^3J_{C\gamma CO}$  and  ${}^3J_{C\gamma N}$  coupling constants obtained for  $\gamma$ -methyl and aromatic residues for each of the complexes are plotted in Figures 4 and 5, together with a comparison of the expected values of each of the fully-populated rotamers, calculated according to the Karplus parameters of Table 1.

### Determination of Preferred Rotamers and Rotamer Populations

When the 3-site rotamer jumping assumption holds, the  ${}^3J_{C\gamma CO}$  and  ${}^3J_{C\gamma N}$  couplings can be converted into rotamer populations according to Eqs. 1–3. To avoid unduly propagating the inherently larger errors of smaller  ${}^3J$  coupling values, the couplings for each residue were first analyzed to determine if observed differences in coupling constants between complexes are statistically significant and therefore reflect different rotamer averaging. In addition to having larger experimental errors, the smaller  ${}^3J$  couplings are also more sensitive to small changes in dihedral angle, since the smallest of the staggered rotamer  ${}^3J$  values tend to occur where the slope of the Karplus curves are the steepest. This is illustrated in Figure 6A, which shows the FWY Karplus curves with shaded areas indicating the  ${}^3J$  values spanned for regions within  $\pm 5^\circ$  of the staggered  $\chi_1$  angles. This  $10^\circ$  range about the expected  ${}^3J$  values is shown on Figures 4 and 5 as blue, green, or red shaded areas for  $J_t$ ,  $J_g$ , and  $J_h$ , respectively. Residues that exhibit variation amongst the complexes in the smaller coupling, but that are tightly clustered for the largest coupling are considered to have equivalent couplings (e.g. Val93). The average couplings across all equivalent complexes for each residue are used to determine the rotamer populations, while populations for residues that differ significantly between complexes are considered based on the experimental couplings for that complex alone. The major rotamer population,  $p_{\text{major}} = \max[p_{-60}, p_{+60}, p_{180}]$ , is a proxy for the extent of rotamer averaging a residue undergoes, whether due to rotamer hopping or due to restricted motions within a rotamer well. In cases where multiple staggered rotamer conformations are unlikely, a reduced value of  $p_{\text{major}}$  indicates increased local rotamer sampling.

Local motions can effectively decrease the expected maximum coupling and broaden the wells in the Karplus correlations. If the local motions can be represented by a Gaussian distribution about a single dihedral angle with variance  $\sigma^2$  (in radians), the averaged  ${}^3J$  coupling can be described by an averaged Karplus curve with the following parameters:<sup>36</sup>

$$A' = A \exp(-2\sigma^2), B' = B \exp(-\sigma^2/2), C' = C + (A - A')/2 \quad (6)$$

An example of the effect of a  $\sigma$  of  $15^\circ$  and  $30^\circ$  on the  ${}^3J_{C\gamma CO}$  and  ${}^3J_{C\gamma N}$  Karplus curves is shown in Figure 6B, where the Karplus curves in the absence of motion are shown as dotted lines, and the effect of increasing local motions is shown by solid and dashed lines.

A comparison of the major rotamer determined from  ${}^3J$  couplings and the x-ray structure  $\chi_1$  angles for each complex is shown in Figure 7. The  $\gamma$ -methyl rotamer populations for each complex and the average values over all complexes are given in Supplementary Tables S1–S9 and the aromatic rotamer populations and their average values are given in Supplementary Tables S10–S18.

### Estimation of Leucine $\chi_2$ Rotamers from Methyl Carbon Chemical Shifts

For Leu side chains, a simple correlation between the  ${}^{13}\text{C}_{\text{methyl}}$  chemical shifts has been proposed to predict  $\chi_2$  rotamer averaging.<sup>24</sup> The stereochemically assigned Leu methyl chemical shifts for the DHFR complexes have been used to give an estimate of the  $\chi_2$  values for the leucine residues in the various complexes of DHFR, and the values are compared with those obtained from the x-ray structures in Figure 8. Full data for all complexes are

shown in Table S19. These values and their variation from those expected for fully-populated staggered rotamers essentially report on the conformational space available to the side chain, and hence provide insights into the environment surrounding each residue.

## DISCUSSION

In unfolded proteins, all side chains undergo  $\chi_1$  rotamer averaging, with populations of *trans*, *gauche<sup>+</sup>*, and *gauche<sup>-</sup>* rotamers that are consistent with the distribution in backbone-dependent rotamer libraries.<sup>37,38</sup> The populations vary between different side chains, reflecting differences in bulk and potential for steric clash with backbone heavy atoms, principally the carbonyl oxygen. In the core of well-structured proteins, the extent of rotamer averaging diminishes in a manner proportional to the size of the side chain due to a reduction in the available conformational space. Rotamer populations of folded proteins report on the extent to which a particular rotamer is stabilized and/or that other rotamers are destabilized due to steric clash with nearby groups or hydrogen bonding interactions. Due to the large size of aromatic side chains, this usually translates to the presence of one predominant rotamer. The smaller methyl-containing side chains frequently maintain some rotamer averaging in the core of a folded protein, though generally to a lower extent than in the random coil state. Information on the rotameric states of side chains can be obtained by measuring three-bond couplings,  $^3J_{C\gamma CO}$  and  $^3J_{C\gamma N}$  (Figure 1C). By combining this experimental information with empirical analysis of rotamer states obtained from Karplus curves, an estimate of the populations of  $\chi_1$  rotamers can be obtained.

The extent of rotamer averaging is plotted on the structure of E:FOL:NADP<sup>+</sup> (PDB: 3QL3) in Figure 9. Aromatic and methyl side chains with the same rotamer averaging across all DHFR complexes, are shown by spheres colored with a white to red gradient, where more red indicates a greater extent of averaging (i.e., a smaller  $p_{\text{major}}$ ). Residues that populate different rotamers or display different rotamer averaging in one or more of the DHFR complexes are colored in green; these will be discussed in greater detail below. This approach to the analysis is especially suited to comparison of extent of averaging for different residues within each complex, or between the same residue in different complexes.

### Side Chains with the Same Rotamer Averaging across all Complexes

A comparison of the extent of side chain rotamer averaging for each of the *E. coli* DHFR complexes shows that the majority of residues for which data are available are invariant to the nature of the bound ligands. These include numerous methyl residues in the adenosine binding domain that show basal levels of averaging between different rotamers. When bulky methyl-containing amino acids such as Ile and Val are located in close proximity in the hydrophobic core, they show similar levels of rotamer averaging. The aromatic residues within this invariant subset are almost all in one predominant rotamer; however many of the  $^3J$  measurements for the aromatics indicate some level of in-well averaging.

**Rotamer Averaging of Ile, Val, and Thr Side Chains**—Ile and Val residues that are in close proximity to each other – and are not in flexible loop regions – have similar levels of rotamer averaging. The average  $p_{\text{major}}$  of all Ile, Thr, and Val residues in the adenosine domain is  $88 \pm 6\%$ . Notably, the two residues in the adenosine domain with the least rotamer averaging (Val88 and Val99), are somewhat isolated from these other methyl residues. In particular, Val88 shows very little rotamer averaging, with average  $p_{\text{major}}$  across all complexes of 97% (range: 94–98%). The Val99 side chain lines part of the binding pocket for the adenosine moiety of NADP/H and so may be expected to display different rotamer averaging in the presence or absence of cofactor; however, very little rotamer averaging is observed in any of the complexes ( $p_{\text{major}}$  95%, range 79–98%). Amongst the

other Leu and Val residues, Ile60 and Ile41, located in the core of the adenosine domain, have the least rotamer averaging with  $p_{\text{major}}$  of 90% (82–90%) and 89% (86–90%), respectively. Ile2, Ile91, Ile82, Val78, and Val93 are located around these core residues and have  $p_{\text{major}}$  values ranging from 81 to 85%. Similar levels of rotamer averaging are also seen for proximal residues in the loop subdomain. In particular, Val136 and Ile155, which are in adjacent beta strands, have major populations of 84% (81–88%) and 88% (82–90%), respectively.

### Rotamer Averaging of Aromatic Side Chains

Of the residues with invariant rotamer averaging across the series of complexes, Phe140 is the only aromatic side chain that clearly averages over multiple staggered rotamer conformations, as indicated by the intermediate values of both  ${}^3J_{C\gamma CO}$  and  ${}^3J_{C\gamma N}$  couplings. It is solvent exposed, and the local structure is such that any of the staggered conformations could be accommodated, as is demonstrated by the different  $\chi_1$  conformations built in the x-ray structures of the DHFR complexes (Figure 7). The Phe 140 coupling constants vary little between complexes and their average indicates a major rotamer population of 51%  $\chi_1=180^\circ$  with the remainder split between the  $\pm 60^\circ$  rotamers. For Phe137, the intermediate and tightly clustered  ${}^3J_{C\gamma N}$  values for the various complexes indicates significant rotamer averaging, with the  $\chi_1 = 180^\circ$  rotamer dominant. Inspection of the structure indicates that there would be significant steric clashes in the  $+60^\circ$  rotamer. Additionally, the  ${}^3J_{C\gamma CO}$  coupling for Phe137 does not increase in a way to suggest significant populations of  $-60^\circ$  rotamer. The region between  $180^\circ$  and  $-60^\circ$  rotamers is solvent exposed, and therefore conformationally accessible, but as the side chain approaches the classical  $-60^\circ$  rotamer, steric clashing would occur with the neighboring Val136 carbonyl oxygen. The decreased  ${}^3J_{C\gamma N}$  (relative to  $J_t$ ), combined with the lack of an increase in  ${}^3J_{C\gamma CO}$  (relative to  $J_h$ ), suggests a dominant  $180^\circ$  rotamer with asymmetric conformational sampling in the region between a  $\chi_1$  of  $180^\circ$  and  $-60^\circ$ ; this is consistent with the shape of the Karplus curves at  $180^\circ$  (see Figure 6).

The other aromatic side chains show much less rotamer averaging than Phe137 or Phe140. Trp74, Tyr111, and Tyr128 appear to be the most conformationally restricted of the aromatic side chains. The remaining aromatic side chains with similar rotamer behavior in all complexes show some small amount of rotamer averaging, most likely due to conformational sampling within a single rotamer well. For Trp22,  ${}^3J_{C\gamma CO}$  and  ${}^3J_{C\gamma N}$  are both very small ( $0.71 \pm 0.19$  and  $0.68 \pm 0.21$  Hz, respectively), indicating a predominantly  $+60^\circ$  conformation, but these couplings are somewhat larger than expected for a fully  $+60^\circ$  rotamer ( $J_g$  of 0.55 and 0.38 Hz, respectively). Given that Trp22 is deeply buried in the active site and is involved in a conserved, water mediated hydrogen bond network, averaging with alternative  $\chi_1$  rotamers is highly improbable, since both  $+60^\circ$  and  $180^\circ$  conformations would result in extreme steric clashes and would expose the Trp side chain to solvent. A more likely explanation for the increased couplings is conformational sampling by fluctuations within the  $\chi_1 = +60^\circ$  rotamer well; examination of x-ray structures for the wild type DHFR complexes studied suggests that the Trp22 side chain can move substantially and without steric clash by averaging about  $\chi_1$ . The major rotamer population determined from Eqs. 1–3 is still a reasonable measure of this extent of this restricted conformational sampling, since it is a measure of the deviation of the couplings from the expected maximum and minimum values. Therefore, the increased red coloring in Figure 9 of, for example, Trp22 and Phe137, is indicative of more extensive rotamer averaging within a single well than for the lighter colored aromatic side chains.

## Side Chains with Complex-dependent Rotamer Averaging

The residues colored in green in Figure 9 have  $^3J_{C\gamma CO}$  and  $^3J_{C\gamma N}$  values that are unique in one or more of the *E. coli* DHFR complexes studied or have Leu  $^{13}C$  methyl chemical shifts that indicate differences in rotamer averaging between complexes. These residues are primarily near the ligand binding sites, with most of the residues with complex-dependent averaging clustering around the active site. Variable methyl rotamer averaging is seen for Ile14, Leu28, Val40, Thr46, Ile50, Leu54, Leu62, Val75, Ile94, Val119, and Thr123, and for the aromatic residues His45, Tyr100, His124, and His149. The following paragraphs provide a brief summary of the behavior of some of these side chains. A more comprehensive discussion of the results for individual side chains is given in the Supplementary Material.

One of the most variable of the side-chains is Ile14, which shows near-100% population of the  $+60^\circ \chi_1$  rotamer in all complexes except E:NADPH and E:FOL and near-50:50 mixture of the  $+60^\circ$  and  $-60^\circ$  rotamers in the E:NADPH and E:FOL complexes. The backbone structure of Ile14 in the occluded DHFR x-ray structures favors the  $+60^\circ \chi_1$  rotamer<sup>15</sup> (blue point in Figure S2). The  $^3J$  couplings of E:NADPH and E:FOL are consistent with either averaging with the  $-60^\circ$  rotamer or local averaging within the  $+60^\circ$  rotamer well. Based on the x-ray structure of E:NADPH (1RX1), the  $-60^\circ$  rotamer would result in steric clash between C $\gamma$ 2 of Ile14 and the nicotinamide ring of NADPH and some motions must occur to accommodate this minor rotamer. The greater extent of averaging for Ile14 in E:NADPH likely arises from decreased crowding in the active site in the absence of substrate, and from motions of the active site loops. While for most residues rotamer averaging is similar for E:THF and the analogue E:FOL, there is significant difference for Ile14. Although the x-ray structures of E:FOL and E:THF are essentially identical in the active site loops, there are significant differences in the backbone dynamics: numerous residues in the E:FOL Met20 loop show relaxation dispersion over a broad range of temperatures, while E:THF shows dispersion for only Ala19 at 303 K and higher.<sup>5</sup> These differences in loop motions are expected to contribute to the rotamer averaging observed in E:FOL for Ile14. Contrary to our previous report,<sup>9</sup> neither Ile94 nor Ile14 are found to have any significant  $\chi_1 = 180^\circ$  rotamer subpopulation in the E:FOL:NADP $^+$  complex. Errors in the previous measurements appear to have arisen from a miscalibrated  $^{13}C$  carbonyl inversion shaped pulse, which led to the systematic underestimation of the  $^3J_{C\gamma CO}$  values and the subsequent impact on calculated rotamer populations.

For Val119, the differences in the extent of rotamer averaging can be directly ascribed to the presence of a closed or occluded complex. Little rotamer averaging occurs in closed complexes, with average  $p_{\text{major}} = 92\%$  in the  $\chi_1 = -60^\circ$  rotamer. The occluded complexes exhibit extensive rotamer averaging, with an average population of 41% in  $\chi_1 = 180^\circ$  rotamer and with the remaining population split between the  $\pm 60^\circ$  rotamers. Large amplitude motions on a ps/ns timescale were observed for residues within the Met20 and F-G loops in occluded complexes, motions that are attenuated for closed complexes.<sup>11</sup> The greater degree of available space, together with loss of crucial hydrogen bonds in the occluded complexes, likely contribute to the enhanced backbone dynamics in the active site loops, leading to the extensive rotamer averaging seen in occluded complexes.

The side chain of Tyr100 is tightly packed in the active site, forming hydrogen bonds through its hydroxyl group to Ile5-CO, Ile94-CO, the C4 atom of the nicotinamide ring for closed complexes (this is the proton donor for the reduction of DHF to THF), and the N8 atom of the pterin ring of THF when THF is bound. The large  $^3J_{C\gamma CO}$  and small  $^3J_{C\gamma N}$  show that  $\chi_1$  lies within the *gauche* $^-$  ( $-60^\circ$ ) rotamer well. Variations in coupling constants amongst complexes likely reflect differences in  $\chi_1$  fluctuations within the *gauche* $^-$  well, adoption of non-canonical  $\chi_1$  angles, or some combination of both. Rotamer averaging with the *gauche* $^+$  or *trans* wells is extremely unlikely; the x-ray structures indicate that these

alternate rotamers would lead to severe steric clashes of the Tyr100 side chain. We note that Tyr100 has skewed  $\chi_1$  angles (between  $-79^\circ$  and  $-90^\circ$ ) in the x-ray structures of all of the wild type *E. coli* DHFR complexes (Tables S11–S18).

### Changes in Rotamer Averaging through the DHFR Catalytic cycle

The changes in rotamer states and the extent of rotamer averaging between the various DHFR complexes can be rationalized with reference to the changes that occur between adjacent complexes in the catalytic cycle, as illustrated in Figure 10.

**E:NADPH to E:FOL:NADP<sup>+</sup>**—Relative to the E:FOL:NADP<sup>+</sup> complex, E:NADPH shows strikingly greater motional averaging in residues located along the plane dividing the adenosine binding domain and active site loop regions. Increased averaging about  $\chi_1$  is observed for Ile14, Ile50, Tyr100, and His124, and about  $\chi_2$  for Leu54 (red residues in Figure 10). The coupling constants suggest that Ile94 exhibits a comparable extent of  $\chi_1$  averaging in both complexes but the major rotamer differs ( $\chi_1 = -60^\circ$  for E:NADPH in solution,  $\chi_1 = +60^\circ$  for E:FOL:NADP<sup>+</sup> and also in the x-ray structure of the E:NADPH complex). We note that the  $\chi_1 = -60^\circ$  rotamer would cause the Ile94  $\gamma$ 2 methyl to clash with the pterin ring in the E:FOL:NADP<sup>+</sup> complex so this state is only favorable when the substrate/product binding site is empty; it is likely that Ile94 undergoes averaging within the  $+60^\circ$  rotamer well in complexes with bound folate or THF, rather than averaging with the  $\chi_1 = -60^\circ$  rotameric state. The nicotinamide ring of NADPH, which bridges the two domains of DHFR, and the backbone of the Met20 loop also show an increased level of disorder in E:NADPH relative to the E:FOL:NADP<sup>+</sup>, as evidenced by x-ray B-factors.<sup>3</sup> For the residues in direct contact with the cofactor (Ile14 and Tyr100), the apparent increase in rotamer averaging (decreased  $^3J_{C\gamma CO}$ ) in the E:NADPH complex most likely reflects increased fluctuations within the dominant  $\chi_1$  rotamer well rather than jumps to one of the alternative rotameric states, which the x-ray structures suggest would be sterically unfavorable. However, Ile50 ( $\chi_1$ ) and Leu54 ( $\chi_2$ ), which line one face of the substrate/product binding site, exhibit increased rotamer averaging in the E:NADPH complex where this binding site is vacant. Increased  $\chi_2$  rotamer averaging is also observed for Leu28 on the opposite side of the empty substrate binding pocket. The flexibility of certain side chains that line the walls of the empty binding pocket in the E:NADPH holoenzyme may play a functional role in facilitating capture and binding of incoming substrate.

**E:FOL:NADP<sup>+</sup> to E:THF:NADP<sup>+</sup>**—The most notable difference in rotamer averaging between the Michaelis model complex and the product ternary complex is for Val119, which reflects the closed to occluded transition as discussed above. Most residues display a very similar level of rotamer averaging in these two complexes. However, His45 and Ile50 exhibit slightly higher flexibility in the E:THF:NADP<sup>+</sup> product complex, while Leu28 and Leu62 show a slight decrease in  $\chi_2$  rotamer averaging. The rotamer averaging for these residues appears to be sensitive to the nature of the bound ligand; the Leu62  $\chi_1$  angle in the x-ray structures of E:FOL:NADP<sup>+</sup> and E:MTX:NADPH (Table S19) differs from that in the other complexes and allows averaging about  $\chi_2$ , which is disfavored due to steric clash with the adenosine ring in the E:NADPH and E:THF:NADP/H complexes.

**E:THF:NADP<sup>+</sup> to E:THF and E:THF to E:THF:NADPH**—The ternary product complexes are essentially indistinguishable in their NMR spectra and measured  $^3J$  couplings. Comparison of these complexes to the product binary complex E:THF primarily reveals an increase in flexibility in the E:THF complex in the absence of cofactor. This is most significant for His45 which can sample multiple rotamers when the cofactor binding site is vacant. His124 is expected to show in-well rotamer averaging as for E:NADPH, and Leu62 changes major  $\chi_2$  rotamer from  $180^\circ$  for the ternary complexes to  $+60^\circ$  in E:THF.

**E:THF:NADPH to E:NADPH**—The product release complex E:THF:NADPH shows significantly less rotamer averaging than the holoenzyme E:NADPH. This is particularly true for residues in the plane dividing the adenosine and active site loop domains, which with the exception of Ile50 also exhibited altered rotamer averaging in E:NADPH relative to E:FOL:NADP<sup>+</sup>.

**E:MTX:NADPH to E:FOL:NADP<sup>+</sup>**—The transition state model E:MTX:NADPH has very similar levels of rotamer averaging as the Michaelis model complex E:FOL:NADP<sup>+</sup> (Figure 10). The most significant difference is for Tyr100, which is highly sensitive to the nature of the bound ligands and shows more in-well rotamer averaging or a differently skewed rotamer for the E:MTX:NADPH complex.

**N23PP/S148A to WT E:FOL:NADP<sup>+</sup>**—Mutant and wildtype E:FOL:NADP<sup>+</sup> exhibit highly similar levels of rotamer averaging throughout the protein (Figure 10). Slight differences for Tyr100, Leu28, and Trp30 may be indicative of minor changes in the active site packing for the mutant relative to the wild-type E:FOL:NADP<sup>+</sup> complex.

**E:FOL to E:THF**—The extent of rotamer averaging between the substrate analogue and product binary complexes is most different for residues near the cofactor binding site (Figure 10). E:FOL shows an increase in rotamer averaging for His124, Ile14, Tyr100, and His45, which are all proximal to the cofactor binding site, and for Ile61 in the adenosine binding domain. There are additional subtle differences around FOL/THF, which further demonstrates the sensitivity of *E. coli* DHFR to the nature of the bound ligand.

### Comparison with S<sup>2</sup><sub>axis</sub>

Correlations between p<sub>major</sub> and the side chain order parameter S<sup>2</sup><sub>axis</sub> have been proposed previously.<sup>39,40</sup> However, we find no significant correlation between the p<sub>major</sub> values and published methyl order parameters for E:FOL and E:FOL:NADP<sup>+</sup>.<sup>9</sup> Most of the S<sup>2</sup><sub>axis</sub> values reported are larger than 0.7 and are not predictive of the degree of rotamer averaging found. In the case of Val119 in the E:FOL complex, S<sup>2</sup><sub>axis</sub> is small (0.27 for C<sub>γ</sub>1 and 0.25 for C<sub>γ</sub>2) which correlates well with the high degree of rotamer averaging observed from the coupling constants, with each staggered rotamer significantly populated. In contrast, however, Val119 also has a low S<sup>2</sup><sub>axis</sub> value (0.45 for C<sub>γ</sub>2) in E:FOL:NADP<sup>+</sup>, yet the side chain exhibits a very low level of  $\chi_1$  rotamer averaging (p<sub>major</sub> = 0.88). The lack of a correlation between S<sup>2</sup><sub>axis</sub> and p<sub>major</sub> likely reflects the mismatch of timescales on which the methods report (picosecond timescale motions for S<sup>2</sup><sub>axis</sub> versus a broad ps-ms timescale for <sup>3</sup>J couplings) and also the fact that S<sup>2</sup><sub>axis</sub> is sensitive to fast timescale motions that may not involve change in the  $\chi_1$  dihedral angle, which is the primary contribution to the <sup>3</sup>J value.

## CONCLUSIONS

To our knowledge, the current set of <sup>3</sup>J<sub>C<sub>γ</sub>CO</sub> and <sup>3</sup>J<sub>C<sub>γ</sub>N</sub> coupling constants for 8 *E.coli* DHFR complexes is the most complete set of data available for any protein. These data provide valuable insights into determinants of side chain rotamer averaging and into the uncertainties inherent in interpretation of coupling constant data using rotamer jump models. From the point of view of protein structure, it is striking that the rotameric states of the vast majority of side chains probed (12 Ile, 11 Val, 6 Thr, 11 Leu (at  $\chi_2$ ), 5 Trp, 6 Phe, 4 Tyr, and 5 His) populate a dominant rotameric state that is determined primarily by the protein fold and packing of the hydrophobic core (Figure 5). Nevertheless, a subset of side chains do undergo changes in rotamer or exhibit rotamer averaging in response to binding of different ligands or backbone conformational change.

The current data indicate the need for considerable caution in the interpretation of  $^3J_{C\gamma CO}$  and  $^3J_{C\gamma N}$  coupling constants and demonstrate emphatically that the assumption of a simple 3-site rotamer jump model is not always valid. Firstly, the availability of such a large number of independently measured coupling constants for a series of related complexes of known 3D structure allowed us to reevaluate existing Karplus parameterizations for both aliphatic and aromatic side chains. Secondly, the uncertainties inherent in measurement of  $^3J_{C\gamma CO}$  and  $^3J_{C\gamma N}$  coupling constants, at least for a protein as large as DHFR (18 kDa), suggest a need for caution in interpreting small differences in terms of changes in rotamer averaging, especially in the case where both couplings are small and the errors are correspondingly large. Thirdly, we frequently observed substantial variation in the magnitude of the coupling constants for a given residue in different complexes, even when it was clear that the side chain was predominantly in the same rotamer well in each complex and when steric considerations made averaging over other rotameric states improbable, e.g. for Trp22 or Tyr100. Indeed, we found that the  $^3J$  couplings can be extremely sensitive to small variations in the structure of both the protein and the nature of the bound ligands. It is important to interpret the experimental coupling constants for each residue within the context of its environment within the protein: does a rotamer averaging model make sense, with only minimal steric clash in one or both of the alternative rotameric states, or are the data better interpreted in terms of averaging within a single rotamer well? In this regard we note that certain side chains may be constrained to non-classical rotamer angles (e.g. Tyr100 is tightly packed in the active site, with  $\chi_1$  between  $-79$  and  $-90^\circ$  in the x-ray structures of the wild type *E. coli* complexes) and may undergo asymmetric conformational averaging within their energy wells. All of these factors need to be taken into consideration for meaningful interpretation of NMR coupling constants.

## Supplementary Material

Refer to Web version on PubMed Central for supplementary material.

## Acknowledgments

### Funding

This work was supported by grant GM75995 from the National Institutes of Health.

We thank Gerard Kroon for his assistance in setting up the required NMR coupling experiments and Maria Yamout-Martinez and Gira Bhabha for their assistance in sample preparation.

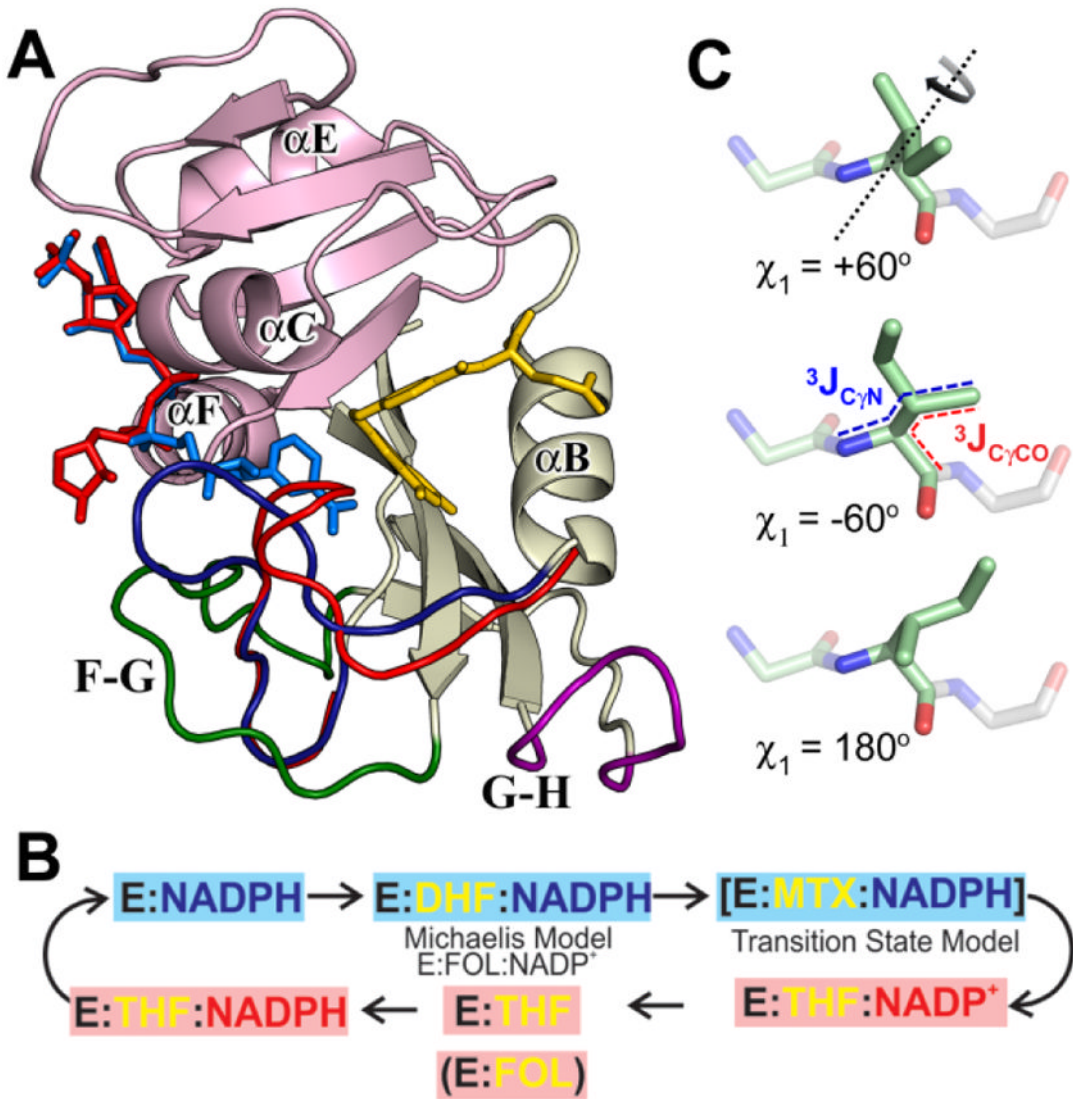
## ABBREVIATIONS

<b>DHFR</b>	dihydrofolate reductase
<b>NADP<sup>+</sup></b>	nicotinamide adenine dinucleotide phosphate
<b>NADPH</b>	reduced nicotinamide adenine dinucleotide phosphate
<b>DHF</b>	7,8-dihydrofolate
<b>THF</b>	(6S)-5,6,7,8-tetrahydrofolate
<b>FOL</b>	folate
<b>MTX</b>	methotrexate
<b>NMR</b>	nuclear magnetic resonance
<b>HSQC</b>	heteronuclear single quantum correlation

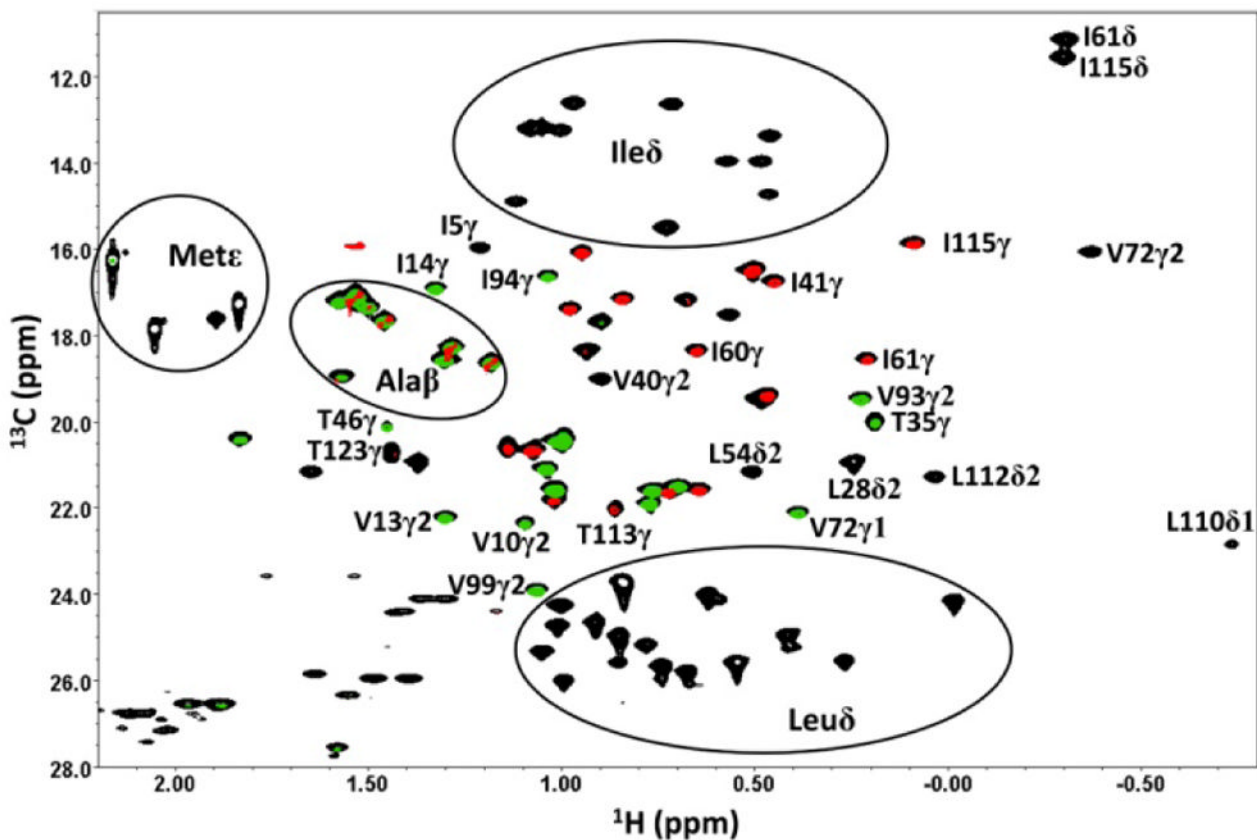
## References

1. Bystroff C, Oatley SJ, Kraut J. Crystal structures of *Escherichia coli* dihydrofolate reductase: the NADP<sup>+</sup> holoenzyme and the folate-NADP<sup>+</sup> ternary complex. Substrate binding and a model for the transition state. *Biochemistry*. 1990; 29:3263–3277. [PubMed: 2185835]
2. Bystroff C, Kraut J. Crystal structure of unliganded *Escherichia coli* dihydrofolate reductase. Ligand-induced conformational changes and cooperativity in binding. *Biochemistry*. 1991; 30:2227–2239. [PubMed: 1998681]
3. Sawaya MR, Kraut J. Loop and subdomain movements in the mechanism of *Escherichia coli* dihydrofolate reductase: crystallographic evidence. *Biochemistry*. 1997; 36:586–603. [PubMed: 9012674]
4. Schnell JR, Dyson HJ, Wright PE. Structure, dynamics and catalytic function of dihydrofolate reductase. *Ann Rev Biophys Biomol Struct*. 2004; 33:119–140. [PubMed: 15139807]
5. Boehr DD, McElheny D, Dyson HJ, Wright PE. Millisecond timescale fluctuations in dihydrofolate reductase are exquisitely sensitive to the bound ligands. *Proceedings of the National Academy of Sciences*. 2010; 107:1373–1378.
6. Boehr DD, McElheny D, Dyson HJ, Wright PE. The dynamic energy landscape of dihydrofolate reductase catalysis. *Science*. 2006; 313:1638–1642. [PubMed: 16973882]
7. Mittermaier A, Kay LE, Forman-Kay JD. Analysis of deuterium relaxation-derived methyl axis order parameters and correlation with local structure. *J Biomol NMR*. 1999; 13:181–185. [PubMed: 20700817]
8. Wand AJ, Urbauer JL, McEvoy RP, Bieber RJ. Internal dynamics of human ubiquitin revealed by <sup>13</sup>C-relaxation studies of randomly fractionally labeled protein. *Biochemistry*. 1996; 35:6116–6125. [PubMed: 8634254]
9. Schnell JR, Dyson HJ, Wright PE. Effect of cofactor binding and loop conformation on side chain methyl dynamics in dihydrofolate reductase. *Biochemistry*. 2004; 43:374–383. [PubMed: 14717591]
10. Fraser JS, van den Bedem H, Samelson AJ, Lang PT, Holton JM, Echols N, Alber T. Accessing protein conformational ensembles using room-temperature X-ray crystallography. *Proc Natl Acad Sci U S A*. 2011; 108:16247–16252. [PubMed: 21918110]
11. Osborne MJ, Schnell J, Benkovic SJ, Dyson HJ, Wright PE. Backbone dynamics in dihydrofolate reductase complexes: Role of loop flexibility in the catalytic mechanism. *Biochemistry*. 2001; 40:9846–9859. [PubMed: 11502178]
12. Radkiewicz JL, Brooks CL. Protein dynamics in enzymatic catalysis: Exploration of dihydrofolate reductase. *J Am Chem Soc*. 2000; 122:225–231.
13. Agarwal PK, Billeter SR, Rajagopalan PTR, Benkovic SJ, Hammes-Schiffer S. Network of coupled promoting motions in enzyme catalysis. *Proc Natl Acad Sci USA*. 2002; 99:2794–2799. [PubMed: 11867722]
14. Chou JJ, Case DA, Bax A. Insights into the mobility of methyl-bearing side chains in proteins from (3)J(CC) and (3)J(CN) couplings. *J Am Chem Soc*. 2003; 125:8959–8966. [PubMed: 12862493]
15. Shapovalov MV, Dunbrack RL Jr. A smoothed backbone-dependent rotamer library for proteins derived from adaptive kernel density estimates and regressions. *Structure*. 2011; 19:844–858. [PubMed: 21645855]
16. MacArthur MW, Thornton JM. Protein side-chain conformation: a systematic variation of chi 1 mean values with resolution - a consequence of multiple rotameric states? *Acta Crystallogr D Biol Crystallogr*. 1999; 55:994–1004. [PubMed: 10216296]
17. Shapovalov MV, Dunbrack RL Jr. Statistical and conformational analysis of the electron density of protein side chains. *Proteins*. 2007; 66:279–303. [PubMed: 17080462]
18. Karplus M. Vicinal proton coupling in nuclear magnetic resonance. *J Am Chem Soc*. 1963; 85:2870–2871.
19. Schmidt JM. Asymmetric Karplus curves for the protein side-chain 3J couplings. *J Biomol NMR*. 2007; 37:287–301. [PubMed: 17333486]
20. Pachler KGR. Nuclear magnetic resonance study of some [alpha]-amino acids—I: Coupling constants in alkaline and acidic medium. *Spectrochimica Acta*. 1963; 19:2085–2092.

21. Pachler KGR. Nuclear magnetic resonance study of some [alpha]-amino acids--II: Rotational isomerism. *Spectrochimica Acta*. 1964; 20:581–587.
22. Fraser JS, Clarkson MW, Degnan SC, Erion R, Kern D, Alber T. Hidden alternative structures of proline isomerase essential for catalysis. *Nature*. 2009; 462:669–673. [PubMed: 19956261]
23. Bhabha G, Lee J, Ekiert DC, Gam J, Wilson IA, Dyson HJ, Benkovic SJ, Wright PE. A Dynamic Knockout Reveals That Conformational Fluctuations Influence the Chemical Step of Enzyme Catalysis. *Science*. 2011; 332:234–238. [PubMed: 21474759]
24. Mulder FAA. Leucine Side-Chain Conformation and Dynamics in Proteins from  $^{13}\text{C}$  NMR Chemical Shifts. *Chembiochem*. 2009; 10:1477–1479. [PubMed: 19466705]
25. Bhabha G, Tuttle L, Martinez-Yamout MA, Wright PE. Identification of endogenous ligands bound to bacterially expressed human and *E. coli* dihydrofolate reductase by 2D NMR. *FEBS Letters*. 2011; 585:3528–3532. [PubMed: 22024482]
26. Grzesiek S, Anglister J, Bax A. Correlation of backbone amide and aliphatic side chain resonances in  $^{13}\text{C}/^{15}\text{N}$ -enriched proteins by isotropic mixing of  $^{13}\text{C}$  magnetization. *J Magn Reson Series B*. 1993; 101:114–119.
27. Montelione GT, Lyons BA, Emerson SD, Tashiro M. An efficient triple resonance experiment using carbon-13 isotropic mixing for determining sequence-specific resonance assignments of isotopically-enriched proteins. *J Am Chem Soc*. 1992; 114:10974–10975.
28. Grzesiek S, Bax A. Improved 3D triple-resonance NMR techniques applied to a 31 kDa protein. *J Magn Reson*. 1992; 96:432–440.
29. Grzesiek S, Vuister GW, Bax A. A simple and sensitive experiment for measurement of  $\text{J}_{\text{CC}}$  couplings between backbone carbonyl and methyl carbons in isotopically enriched proteins. *J Biomol NMR*. 1993; 3:487–493. [PubMed: 8400833]
30. Vuister GW, Wang AC, Bax A. Measurement of three-bond nitrogen-carbon  $J$  couplings in proteins uniformly enriched in  $^{15}\text{N}$  and  $^{13}\text{C}$ . *J Am Chem Soc*. 1993; 115:5334–5335.
31. Hu JS, Bax A.  $\chi_1$  angle information from a simple two-dimensional NMR experiment that identifies *trans*  $^3\text{J}_{\text{NC}\gamma}$  couplings in isotopically enriched proteins. *J Biomol NMR*. 1997; 9:323–328. [PubMed: 9204558]
32. Hu JS, Grzesiek S, Bax A. Two-dimensional NMR methods for determining  $\chi_1$  angles of aromatic residues in proteins from three-bond  $\text{J}_{\text{C}'\text{C}\gamma}$  and  $\text{J}_{\text{NC}\gamma}$  couplings. *J Am Chem Soc*. 1997; 119:1803–1804.
33. Perez C, Löhr F, Rüterjans H, Schmidt JM. Self-consistent Karplus parametrization of 3J couplings depending on the polypeptide side-chain torsion chi1. *J Am Chem Soc*. 2001; 123:7081–7093. [PubMed: 11459487]
34. Hennig M, Bermel W, Spencer A, Dobson CM, Smith LJ, Schwalbe H. Side-chain conformations in an unfolded protein: chi<sub>1</sub> distributions in denatured hen lysozyme determined by heteronuclear  $^{13}\text{C}$ ,  $^{15}\text{N}$  NMR spectroscopy. *J Mol Biol*. 1999; 288:705–723. [PubMed: 10329174]
35. Xu XP, Case DA. Automated prediction of  $^{15}\text{N}$ ,  $^{13}\text{Ca}$ ,  $^{13}\text{C}\beta$  and  $^{13}\text{C}'$  chemical shifts in proteins using a density functional database. *J Biomol NMR*. 2001; 21:321–333. [PubMed: 11824752]
36. Case DA, Scheurer C, Brüschweiler R. Static and dynamic effects on vicinal scalar  $J$  couplings in proteins and peptides: A MD/DFT analysis. *J Am Chem Soc*. 2000; 122:10390–10397.
37. Vajpai N, Gentner M, Huang, Blackledge M, Grzesiek S. Side-Chain  $\chi_1$  Conformations in Urea-Denatured Ubiquitin and Protein G from 3J Coupling Constants and Residual Dipolar Couplings. *J Am Chem Soc*. 2010; 132:3196–3203. [PubMed: 20155903]
38. Dunbrack RL Jr. Rotamer libraries in the 21st century. *Curr Opin Struct Biol*. 2002; 12:431–440. [PubMed: 12163064]
39. Hu H, Hermans J, Lee AL. Relating side-chain mobility in proteins to rotameric transitions: Insights from molecular dynamics simulations and NMR. *J Biomol NMR*. 2005; 32:151–162. [PubMed: 16034666]
40. Scouras AD, Daggett V. The Dynameomics rotamer library: amino acid side chain conformations and dynamics from comprehensive molecular dynamics simulations in water. *Protein Sci*. 2011; 20:341–352. [PubMed: 21280126]

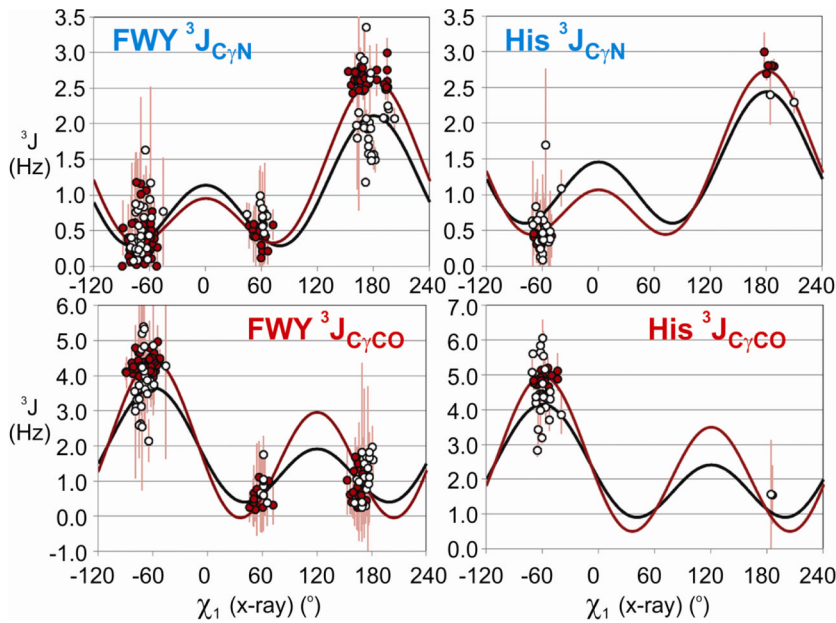
**Figure 1.**

A. Structure of *E. coli* DHFR: adenosine binding domain is shown in pink. Two different structures are superimposed, E:FOL:NADP<sup>+</sup> (1RX2),<sup>3</sup> with the Met20 loop in the closed configuration (shown in blue) and E:THF:NADP<sup>+</sup> (1RX4)<sup>3</sup> with the Met20 loop in the occluded configuration (shown in red). The F-G loop is shown in green, and the G-H loop in purple. Folate (from 1RX2) is shown in yellow; NADP<sup>+</sup> is in blue for the closed state and red for the occluded state, with the nicotinamide ring in a position out of the active site pocket. B. Enzymatic cycle for DHFR, colored according to the superimposed structures in part A. Top row shows the closed complexes; bottom row, occluded. In addition to the intermediates of the catalytic cycle and analogues,  $^3J$  measurements also were obtained for the closed N23PP/S148A E:FOL:NADP<sup>+</sup> complex. C. Schematic showing each of the  $\chi_1$  rotamers (here for isoleucine), with the measured couplings indicated; rotamer populations are calculated based on the measured  $^3J_{C\gamma CO}$  and  $^3J_{C\gamma N}$  values using Eqs 1–3.

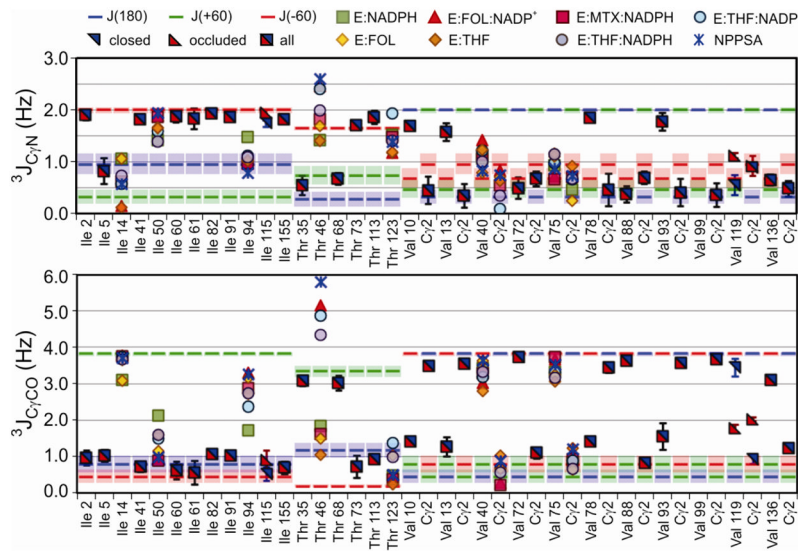


**Figure 2.**

Figure 2. Portion of the  $^{13}\text{C}$  HSQC spectrum of N23PP/S148A E:FOL:NADP+ (black), overlaid with the corresponding portions of the  $\text{C}_\gamma\text{CO}$  (green) and  $\text{C}_\gamma\text{N}$  (red) difference spectra. Only the  $\text{C}_\gamma\text{H}_3$  cross peaks for Ile, Thr, and Val give information in these spectra, although the  $\text{C}_\beta\text{H}_3$  cross peaks of Ala have detectable intensity in the difference spectra. The relative contour levels are 1:0.5:0.25 for the reference,  $^3\text{J}_{\text{C}_\gamma\text{CO}}$  difference, and  $^3\text{J}_{\text{C}_\gamma\text{N}}$  difference spectra, respectively.

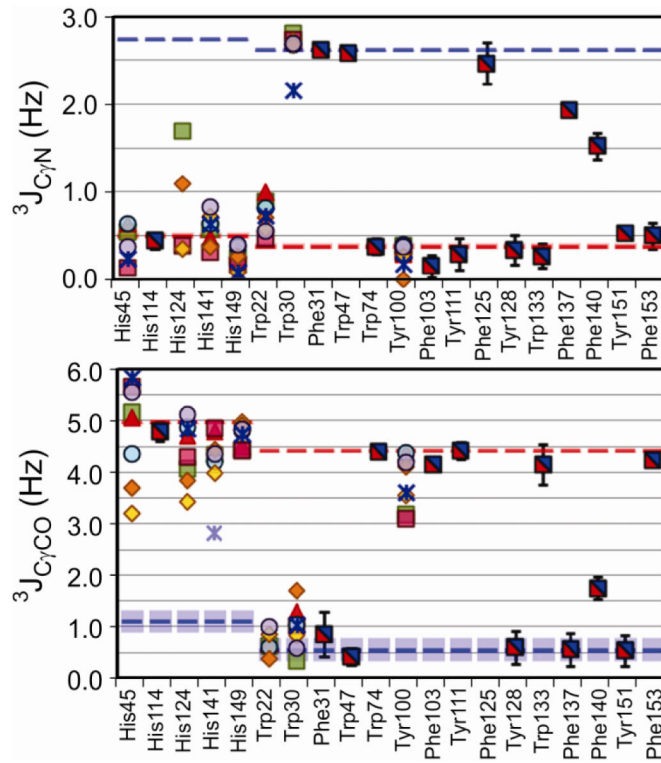
**Figure 3.**

Karplus correlations (plots of  $\chi_1$  angle against  $^3J$ ) for aromatic residues. The  $\chi_1$  angle values are taken from the x-ray crystal structures of E:NADPH (1RX1), E:FOL:NADP<sup>+</sup> (3QL3), E:MTX:NADPH (1RX3), E:THF:NADP/H (1RX4), E:THF (1RX5), E:FOL (1RX7), and N23PP/S148A E:FOL:NADP<sup>+</sup> (3QL0).<sup>3,23</sup> The  $^3J$  values were selected from the data measured in this work for the same complexes in solution. All measured data are plotted. For the least-squares fit to the Karplus equation ( $J = A \cos^2(\theta + \delta) + B \cos(\theta + \delta) + C$ ), only  $^3J$  values for residues without significant rotamer averaging were used. These are indicated by filled circles. Empty circles indicate data with exceptionally large errors or with  $^3J$  couplings that are suggestive of rotamer averaging; these data were excluded from the re-parameterization fits. The black curves in each panel are derived from published Karplus parameters.<sup>19,33</sup> The red curves are derived from the Karplus parameters calculated for the non-averaging aromatic residues in DHFR. Vertical red lines represent the error bars (standard deviations between multiple measurements) for the experimental  $^3J$  values.

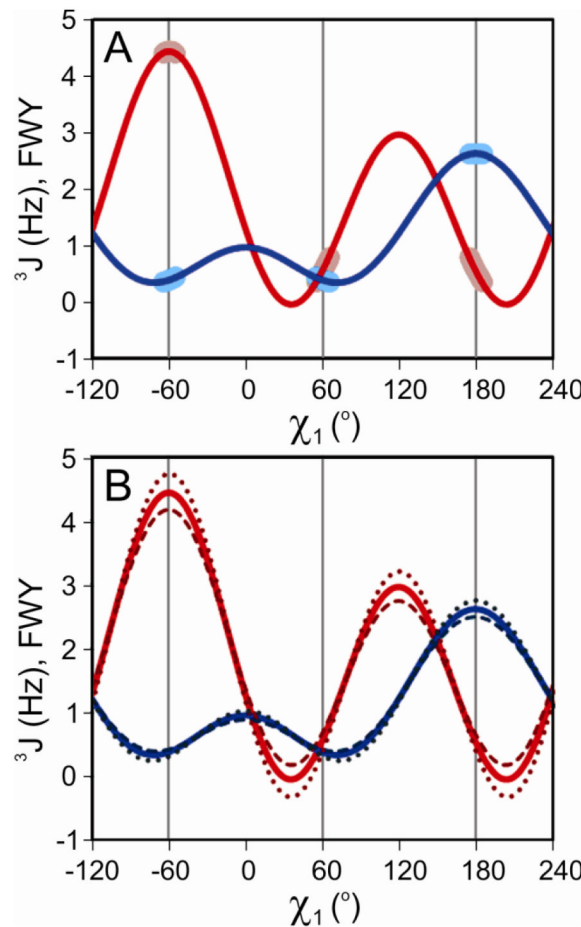


**Figure 4.**

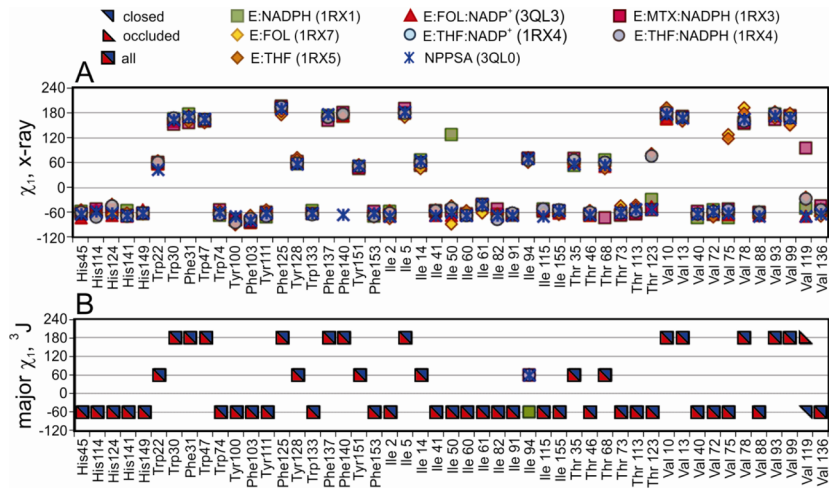
Measured Ile, Thr, and Val methyl  $^3J_{C\gamma CO}$  and  $^3J_{C\gamma N}$  values for the 8 complexes of DHFR, represented by the colored symbols shown. When the values for all complexes have overlapping error ranges, the value is represented by a square halved red and blue, with error bars representing the standard deviation of the values if appropriate. If all occluded or closed complexes have overlapping error ranges, that value is represented by a red or blue triangle respectively. Error bars for individual complexes are left off for clarity (see SI for complete tables with error). NPPSA refers to the N23PP/S148A E:FOL:NADP $^+$  complex. The expectation values  $J_t$ ,  $J_g$ , and  $J_h$  ( $J_{180}$ ,  $J_{+60}$ ,  $J_{-60}$ ) for each residue, derived using the new Karplus parameters, are shown as blue, green, and red bars, respectively, with shaded areas showing a  $\pm 5^\circ$  variation about these values. The following residues are excluded from the ‘All’ complex  $^3J$  averages due to resonance broadening and/or overlap: Ile5, E:THF:NADP/H; Val13 C $\gamma$ 1, closed complexes; Trp47, E:FOL:NADP $^+$ ; Val88 C $\gamma$ 1, E:NADPH and E:THF:NADPH; Val99 C $\gamma$ 1, all complexes; Thr113, THF containing complexes. Thr46 couplings that are aberrantly large in the presence of NADP/H are not interpreted in terms of Eqs 1–3.

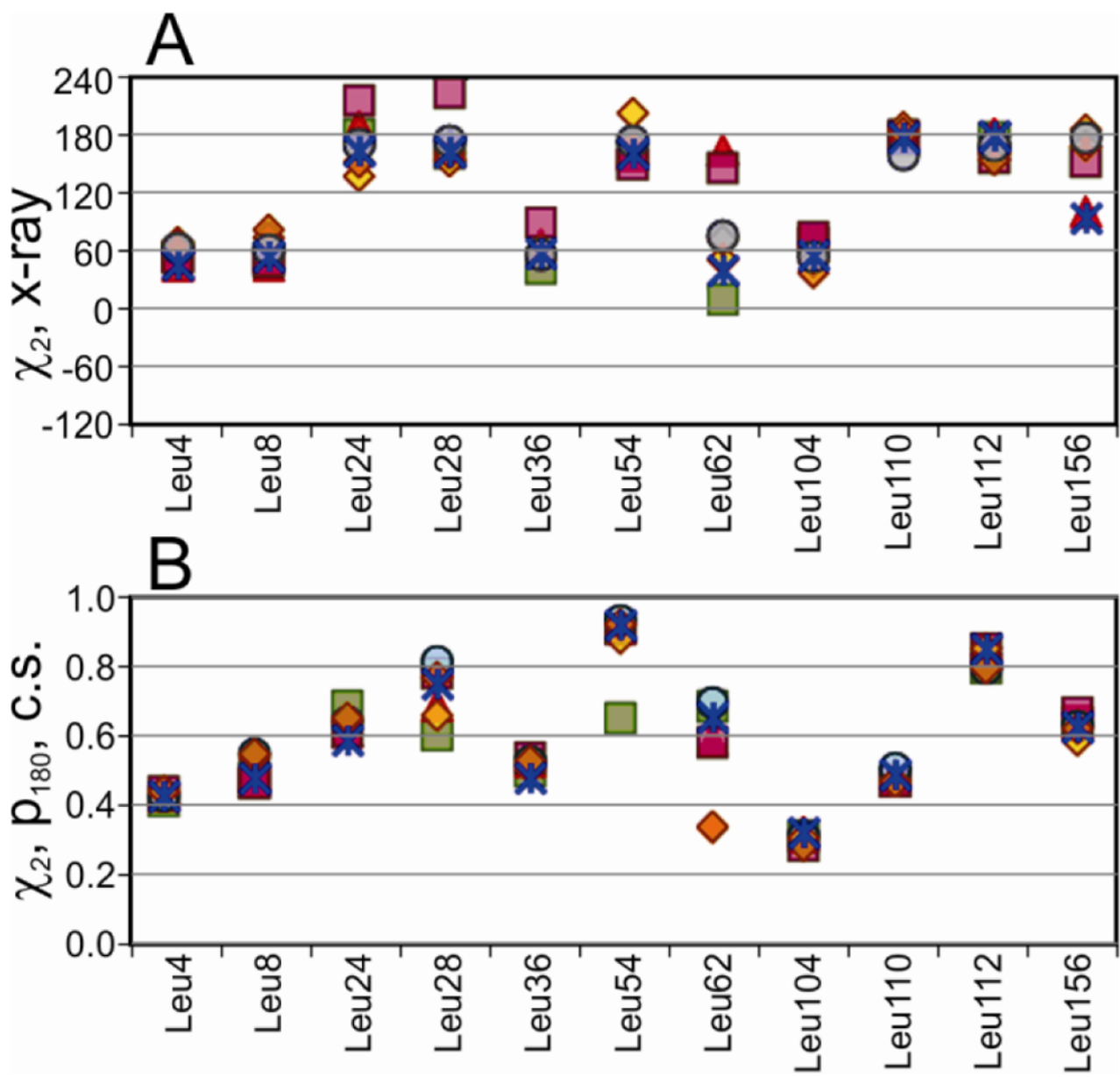
**Figure 5.**

Measured Phe, Trp, Tyr, and His  $^3J_{C\gamma CO}$  and  $^3J_{C\gamma N}$  values for the 8 complexes of DHFR, represented by the colored symbols, groups and expectation values shown at the top of Figure 4. The NPPSA  $^3J_{C\gamma N}$  value for His141 is a lower bound, due to resonance overlap.

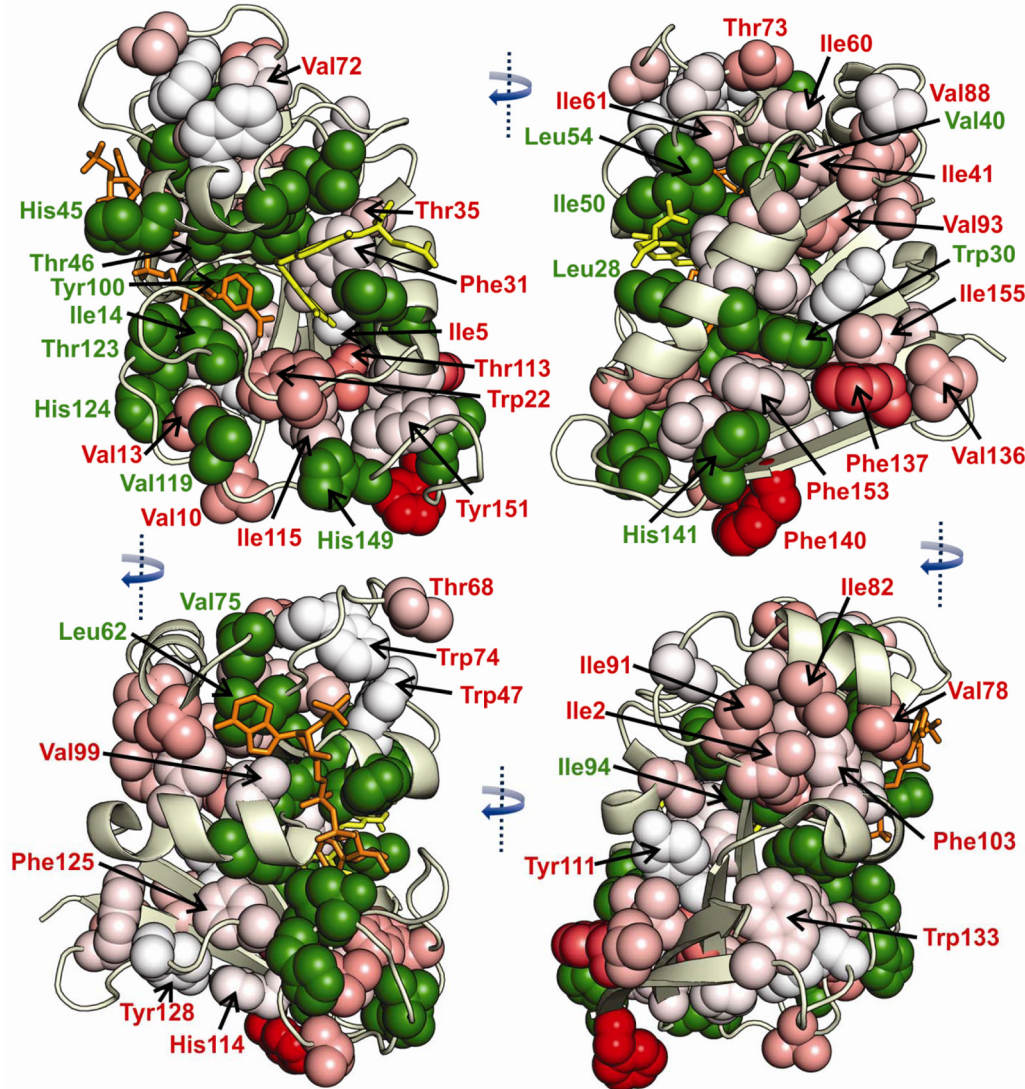


**Figure 6.**  
A.  ${}^3J_{C\gamma CO}$  (red) and  ${}^3J_{C\gamma N}$  (blue) Karplus curves for Phe, Trp, and Tyr residues (FWY), determined from fits of DHFR  ${}^3J$  data. Shaded regions span  $\pm 5^{\circ}$  about the staggered rotamer angles; this variation in  ${}^3J$  is plotted as shaded bars around the  $J_t$ ,  $J_g$ , and  $J_h$  values in Figures 4 and 5. B. Effect of local dynamics on Karplus correlations, according to Eq. 6. Dotted curves illustrate a hypothetical Karplus correlation for fixed side chains. Solid and dashed curves show the effect of Gaussian rotamer sampling with (respectively) 15 $^{\circ}$  and 30 $^{\circ}$  standard deviation relative to the fixed Karplus curve.

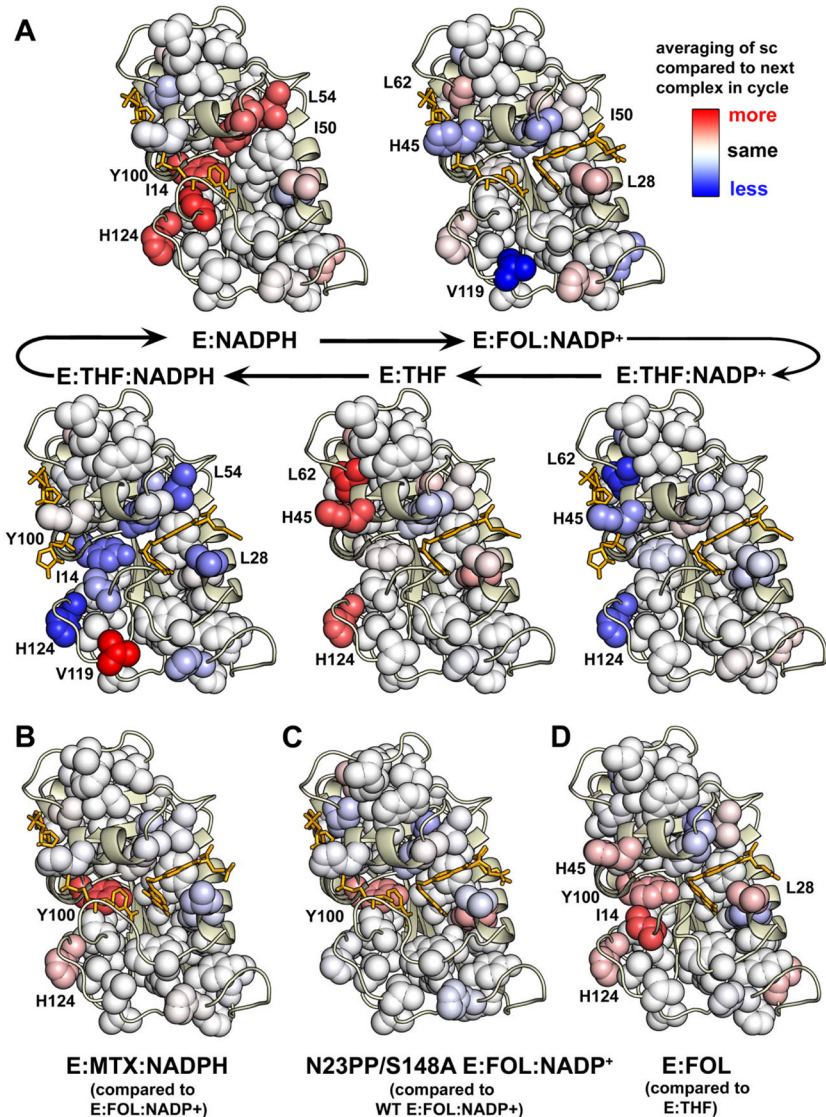


**Figure 8.**

Primary  $\chi_2$  rotamer angle for Leu residues. A. from the x-ray structures (PDB codes shown in Figure 7). B. the chemical shift based population of the 180° rotamer.

**Figure 9.**

Extent of rotamer averaging plotted on the E:FOL:NADP<sup>+</sup> structure (3QL3). Going clockwise, each quadrant shows a 90° rotation about the vertical axis in the plane of the page. FOL is shown as yellow sticks; NADP<sup>+</sup> is orange sticks. Spheres representing side chain heavy atoms are shown for all aromatic, Ile, Thr, and Val residues. Residues with statistically significant variations in rotamer averaging, with uncertainties in <sup>3</sup>J values taken into account, in one or more DHFR complexes are colored green (with green residue labels). Residues that show similar rotamer averaging for each of the DHFR complexes studied are labeled in red and colored white to red to indicate the extent of averaging, with red coloring denoting the most rotamer averaging. The gradient goes from white ( $p_{\text{major}} = 1.0$ ) to red ( $p_{\text{major}} = 0.6$ ), where  $p_{\text{major}} = \max[p_{180}, p_{-60}, p_{+60}]$  as determined according to Eqs 1–3. In cases where rotamer hopping is not expected (e.g. Trp22 and other aromatics), this  $p_{\text{major}}$  is considered a measure of the extent of local motions within a single rotamer well (see Figure 6B for an illustration of the effect this has on <sup>3</sup>J values).

**Figure 10.**

Summary of differences in rotamer averaging between complexes of *E. coli* DHFR. Differences can arise from changes in the extent of rotamer hopping or from changes in local in-well rotamer motions. The corresponding x-ray structure is shown for each complex [E:NADPH (1RX1), E:FOL:NADP<sup>+</sup> (3QL3), E:MTX:NADPH (1RX3), E:THF:NADP/H (1RX4), E:THF (1RX5), E:FOL (1RX7), and N23PP/S148A E:FOL:NADP<sup>+</sup> (3QL0)<sup>3,23</sup>]. Spheres are shown for Ile, Thr, Val, Leu, and aromatic residues. Ligands are shown as sticks with FOL/THF in yellow and NADP/H in orange. A. The difference in  $p_{\text{major}}$  between the given complex and the next complex in the enzymatic cycle is shown for the residues that show variable averaging between complexes (green residues in Figure 9). Side chains with the same rotamer averaging are shown in white, residues with more (less) rotamer averaging than the next complex in the cycle are shown as red (blue), with more red or blue coloring indicating a larger population difference. B. Difference in rotamer averaging between E:MTX:NADPH and E:FOL:NADP<sup>+</sup> complexes. C. Difference in rotamer averaging between N23PP/S148A and wild type E:FOL:NADP<sup>+</sup> complexes. D. Difference in rotamer averaging between E:FOL and E:THF. A–D Leu62, Ile94, and Val119 have a different

major rotamer depending on the complex, so differences in rotamer averaging are given with respect to the  $180^\circ \chi_2$ ,  $+60^\circ \chi_1$  and  $-60^\circ \chi_1$  rotamers, respectively. The color gradient in panels A–D runs from  $\Delta p_{\text{major}} = -0.5$  (blue) < 0 (white) < 0.5 (red), where  $\Delta p_{\text{major}}$  is the difference in major rotamer population between the displayed complex and the next complex in the catalytic cycle (A) or the complex indicated in parentheses (B–D).

Table 1

Table 1A. Karplus parameters used for rotamer averaging analysis<sup>a</sup>

Residue Type	<sup>3</sup> J <sub>CpN</sub>						<sup>3</sup> J <sub>CpCO</sub>		
	A	B	C	$\delta$	A	B	C	$\delta$	
His	1.33	-0.84	0.57	0	3.70	-0.74	0.65	0	
Phe, Trp, Tyr	1.33	-0.84	0.47	0	3.70	-0.74	-0.01	0	
Ile	2.24	0.15	-0.03	-9	3.30	-0.51	0.04	4	
Thr	2.01	0.21	-0.12	7	2.76	-0.67	0.19	17	
Val Cy1	2.22	0.15	-0.06	3	3.30	-0.51	0.04	4	
Val Cy2	2.24	0.15	-0.03	-9	3.30	-0.51	0.04	4	

Table 1B. Predicted values for <sup>3</sup>J couplings at 180°, +60°, and -60°  $\chi_1$  rotamer angles<sup>b</sup>

Residue Type	<sup>3</sup> J <sub>CpN</sub> (Hz)						<sup>3</sup> J <sub>CpCO</sub> (Hz)		
	J <sub>t</sub>	J <sub>g</sub>	J <sub>h</sub>	J <sub>t</sub>	J <sub>g</sub>	J <sub>h</sub>	J <sub>t</sub>	J <sub>g</sub>	J <sub>h</sub>
His	<b>2.73</b>	0.50	0.50	1.09	1.09	1.09	<b>4.97</b>		
Phe, Trp, Tyr	<b>2.62</b>	0.38	0.38	0.55	0.55	0.55	<b>4.43</b>		
Ile	0.95	0.31	<b>2.01</b>	0.79	<b>3.83</b>	0.45			
Thr	0.27	0.73	<b>1.65</b>	1.18	<b>3.35</b>	0.18			
Val Cy1	<b>2.00</b>	0.47	0.68	0.45	0.79	<b>3.83</b>			
Val Cy2	0.31	<b>2.01</b>	0.95	<b>3.83</b>	0.45	0.79			

<sup>a</sup> Karplus parameters for the relationship:  $J = A \cos^2(\theta + \delta) + B \cos(\theta + \delta) + C$ .

<sup>b</sup> Expected <sup>3</sup>J values for fully populated staggered rotamers. All values are given with respect to the  $\chi_1$  angle. Values for the aromatic residues are derived from fits of Karplus curves to the DHFR <sup>3</sup>J data versus the  $\chi_1$  angle in the relevant x-ray structure. Values for the  $\gamma$ -methyl residues are from the parameterizations of Chou et al.<sup>14</sup>.